applied sciences

MDPI

Article

Innovative Data-Driven Machine Learning Approaches for Predicting Sandstone True Triaxial Strength

Rui Zhang, Jian Zhou * and Zhenyu Wang

School of Resources and Safety Engineering, Central South University, Changsha 410083, China; r.zhang@csu.edu.cn (R.Z.); 225512075@csu.edu.cn (Z.W.)
* Correspondence: j.zhou@csu.edu.cn

Abstract: Given the critical role of true triaxial strength assessment in underground rock and soil engineering design and construction, this study explores sandstone true triaxial strength using data-driven machine learning approaches. Fourteen distinct sandstone true triaxial test datasets were collected from the existing literature and randomly divided into training (70%) and testing (30%) sets. A Multilayer Perceptron (MLP) model was developed with uniaxial compressive strength (UCS, σ_c), intermediate principal stress (σ_2), and minimum principal stress (σ_3) as inputs and maximum principal stress (σ_1) at failure as the output. The model was optimized using the Harris hawks optimization (HHO) algorithm to fine-tune hyperparameters. By adjusting the model structure and activation function characteristics, the final model was made continuously differentiable, enhancing its potential for numerical analysis applications. Four HHO-MLP models with different activation functions were trained and validated on the training set. Based on the comparison of prediction accuracy and meridian plane analysis, an HHO-MLP model with high predictive accuracy and meridional behavior consistent with theoretical trends was selected. Compared to five traditional strength criteria (Drucker–Prager, Hoek–Brown, Mogi–Coulomb, modified Lade, and modified Weibols–Cook), the optimized HHO-MLP model demonstrated superior predictive performance on both training and testing datasets. It successfully captured the complete strength variation in principal stress space, showing smooth and continuous failure envelopes on the meridian and deviatoric planes. These results underscore the model's ability to generalize across different stress conditions, highlighting its potential as a powerful tool for predicting the true triaxial strength of sandstone in geotechnical engineering applications.

Keywords: true triaxial strength; failure envelope; HHO; MLP; strength criterion; sandstone

check for updates

Citation: Zhang, R.; Zhou, J.; Wang, Z. Innovative Data-Driven Machine Learning Approaches for Predicting Sandstone True Triaxial Strength. *Appl. Sci.* **2024**, *14*, 7855. https://doi.org/10.3390/app14177855

Academic Editor: Cheng-Yu Ku

Received: 9 August 2024
Revised: 25 August 2024
Accepted: 28 August 2024
Published: 4 September 2024

Copyright: © 2024 by the authors. Licensee MDPI, Basel, Switzerland. This article is an open access article distributed under the terms and conditions of the Creative Commons Attribution (CC BY) license (https://creativecommons.org/licenses/by/4.0/).

1. Introduction

The strength of rocks, considered one of their fundamental mechanical properties, has been extensively investigated by researchers [1–5]. In underground engineering construction, rocks experience a complex true triaxial stress state affected by factors like excavation, original rock stress, and support methods. Consequently, developing a robust true triaxial strength model is paramount for accurately evaluating the true triaxial strength of rocks, which is essential for designing and constructing underground engineering projects. Moreover, the efficacy of numerical simulations in geotechnical engineering hinges significantly on the performance of strength constitutive models.

To achieve this objective, researchers have proposed a range of theoretical and empirical strength criteria by integrating theoretical analyses and laboratory tests, including uniaxial, biaxial, conventional triaxial, and true triaxial strength assessments. Examples of such criteria encompass the Mohr–Coulomb criterion [6], the Hoek–Brown (HB) criterion [7], and the Bieniawski–Yudbir criterion [8], among others. Notably, the Hoek–Brown criterion and the Mohr–Coulomb criterion are extensively utilized in geotechnical engineering analysis and serve as the foundation for rock material constitutive models in numerous

numerical simulation software packages. However, ongoing experimental advancements have revealed that these strength criteria may not be universally applicable across all rock types, stress states, and failure modes.

In particular, the intermediate principal stress significantly influences the true triaxial strength of rocks [9,10]. Consequently, researchers have focused on developing true triaxial strength criteria that account for the impact of the intermediate principal stress. This involves either refining existing strength criteria to comprehensively incorporate the influence factors of the intermediate principal stress or developing entirely new criteria tailored to this consideration. For example, Wu et al. [11] proposed an enhanced Hoek–Brown criterion by integrating the multifunctional offset function with the original Hoek–Brown criterion meridian function. Similarly, Schwartzkopff et al. [12] refined both the Mohr–Coulomb criterion and the Hoek–Brown criterion to incorporate the effects of intermediate principal stress. Da Silva et al. [13] introduced a novel three-dimensional rock strength criterion derived from the Hoek–Brown criterion and the Matsuoka–Nakai criterion. Other strength criteria that take into account the effect of intermediate principal stresses are the Drucker–Prager (DP) criterion [14], the Mogi criterion [15], the Lade–Duncan criterion [16], the modified Weibols–Cook (MWC) criterion [17], the modified Lade (ML) criterion [18], the 3D version of the Hoek–Brown criterion [19], the modified Mohr–Coulomb criterion [20], the Mogi–Coulomb (MGC) criterion [21], etc. Advancements in the true triaxial strength criteria area hold great significance for enhancing the accuracy and reliability of underground engineering design and construction.

Theoretical derivation and conventional data fitting have provided valuable insights into true triaxial damage mechanisms in rock. However, exploration in this area remains limited, leaving much potential for improvement in existing strength criteria. In recent years, spurred by the rapid advancements in computer technology, a plethora of machine learning (ML) models have emerged, offering novel avenues for addressing complex nonlinear problems. In the realm of geotechnical engineering, these ML techniques have found extensive application and garnered notable success in analyzing and predicting intricate engineering issues [22]. Moreover, the prediction of rock strength has become a focal point for numerous scholars, who have increasingly turned to ML methods due to their efficacy and versatility. By leveraging large volumes of rock experimental data for learning and training purposes, ML models can discern intricate patterns underlying rock strength and provide precise predictions. This methodology not only improves the accuracy of rock strength prediction but also mitigates human errors effectively throughout the prediction process. In the study conducted by Fathipour-Azar et al. [23], nine predictive models for rock true triaxial strength were established using six distinct ML algorithms. The research findings suggest that, among these nine models, seven exhibit significant superiority over the existing strength criteria. Furthermore, the enhanced GP model proposed by Yu et al. [24] achieves precise predictions of various rock true triaxial strengths. Similarly, the GEP model developed by Zhou et al. [25] showcases robust generalization capabilities in predicting true triaxial strengths across different rock types. Concurrently, artificial neural network (ANN) models have also seen widespread application in the prediction of rock true triaxial strengths [26–28].

In current research utilizing ML to forecast rock true triaxial strength, several issues have been identified. For instance, the majority of ML models employed by researchers are black-box models, lacking the ability to produce explicit expressions. This limitation hinders the broader extension and application of the derived models. Additionally, some researchers have attempted to address this limitation by creating explicit expressions of the models, leveraging the characteristics of the ML models they utilized. For instance, Rafiai's, Yu's, and Zhou's studies provided explicit expressions of the models. However, due to the limitations of the datasets utilized, wherein stress states predominantly involve compression, Yu's and Zhou's studies failed to accurately predict the true triaxial strength of rocks under tensile principal stress states ($\sigma < 0$). This inadequacy clearly falls short of meeting practical application needs. While Rafiai's ANN model theoretically enables

predictions across various stress states and provides an explicit expression of the model, their study evaluation is confined to comparing the predictive accuracy of the model on the dataset. Consequently, there is a lack of assessment regarding the model's performance in the principal stress space, making it challenging to ascertain whether the predicted trend of strength development under tensile states aligns with theoretical expectations.

For the true triaxial strength model of rocks, it is crucial to satisfy differentiability for further applications in numerical analysis. The Multilayer Perceptron (MLP) model, as a type of feedforward artificial neural network model, is differentiable everywhere except for individual points wherein certain activation functions are used. This provides a foundation for the further expansion of the model's applications. Additionally, the MLP model has shown promising performance in predicting mountain slope failures [29], sand-over-clay bearing capacity [30], and mining-induced stress in underground mines [31].

This study introduces a novel approach by developing a true triaxial strength model for sandstone using a Multilayer Perceptron (MLP) optimized with the Harris hawks optimization (HHO) technique. The MLP model is designed to provide explicit, continuous, and differentiable expressions, which are essential for numerical analysis applications. A dataset comprising 417 sets of true triaxial experimental data for sandstone was collected from the existing literature and randomly divided into a training set (70%) and a testing set (30%). During the model training process, 80% of the training set data were utilized for model training, with the remaining 20% used for validating the model's performance. The traditional strength criterion analysis theories, such as meridian and envelope, were innovatively introduced into the comparative analysis of models, and an HHO-MLP model with excellent prediction accuracy and aligned with the theoretical trend was successfully selected from four HHO-MLP models developed by different activation functions. Comparative analyses with five existing strength criteria revealed that the performance of the HHO-MLP model surpassed that of existing strength criterion models on both the training and testing sets. Further investigation in the principal stress space demonstrated that the failure envelope presented by the HHO-MLP model exhibited good continuity and smoothness, coinciding with different strength criteria in different stress phases.

Additionally, the relationship between the failure envelope and experimental data suggested that the HHO-MLP model provided conservative estimates of sandstone true triaxial strength, but they were not as conservative as the Hoek–Brown criterion. Overall, the HHO-MLP model demonstrated excellent performance in predicting the dataset and presented a failure envelope consistent with theoretical expectations. Furthermore, the model could generate an explicit expression that is continuous and differentiable, ensuring its potential for further extended applications.

2. Methodologies

2.1. Multilayer Perceptron (MLP)

The Multilayer Perceptron (MLP) is a model based on feedforward artificial neural networks, composed of multiple layers of neurons [32]. In an MLP, each neuron layer is fully connected to the preceding layer, and there may be one or more hidden layers between the input and output layers. Each hidden layer consists of multiple neurons, which are defined by activation functions. Common activation functions include sigmoid, tanh, and ReLU. In an MLP model, the connections between neurons in adjacent layers are unidirectional, with the output of neurons in the preceding layer serving as the input for neurons in the subsequent layer. MLP can approximate nonlinear functions with optimal accuracy [33]. Figure 1 illustrates the structure of the MLP model with only one hidden layer and the model operation mechanism. In the figure, $W^{[1]}$ and $W^{[2]}$ denote the weights, $B^{[1]}$ and $B^{[2]}$ denote the biases, and $f_1(x)$ and $f_2(x)$ represent the activation functions.

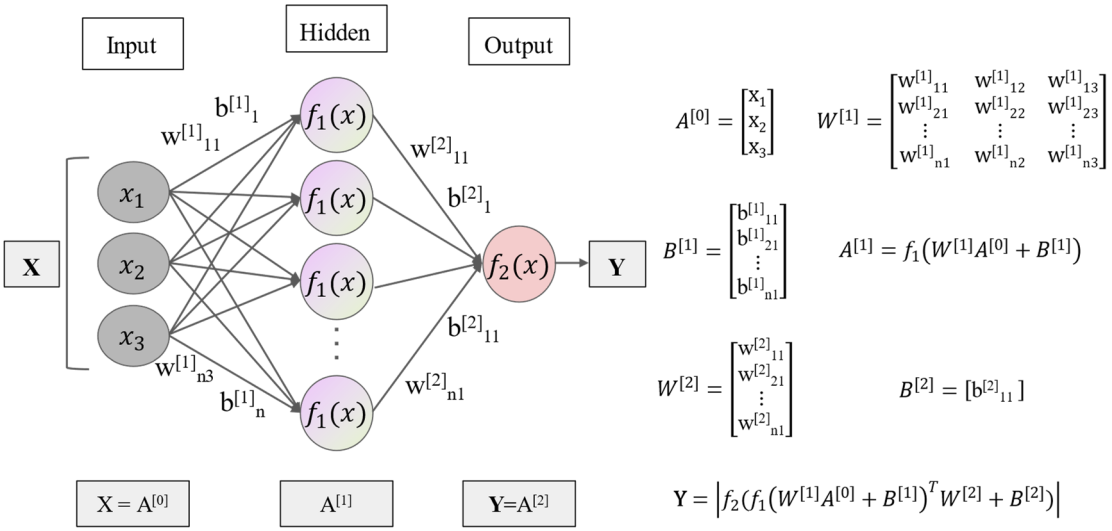

Figure 1. MLP model with only one hidden layer.

2.2. Harris Hawks Optimization (HHO)

The Harris hawks optimization (HHO) algorithm is an optimization technique introduced by Heidari et al. [34], which emulates the predatory behavior of Harris hawks. During this hunting process, Harris hawks operate in groups, with each member undertaking various tasks including tracking, surrounding, approaching, and attacking prey.

Similarly, the HHO algorithm is divided into exploration and exploitation phases during the optimization process. In the exploration phase, HHO utilizes two optimization strategies, as depicted in Equation (1).

$$X_i(t+1) = \begin{cases} X_r(t) - r_1|X_r(t) - 2r_2X_i(t)| \; while \; q \geq 0.5 \\ X_{rabbit}(t) - X_a(t) - r_3(LB + r_4(UB - LB)) \; while \; q < 0.5 \end{cases} \quad (1)$$

$$X_a(t) = \frac{1}{N}\sum_1^N X_i(t) \quad (2)$$

where t represents the iteration number, N denotes the population size of hawks, LB signifies the lower bound of the position, UB represents the upper bound of the position, $X_i(t+1)$ denotes the position of the i hawk at iteration $t+1$, $X_i(t)$ represents the position of the i hawk at iteration t, $X_r(t)$ denotes the position of a random hawk, $X_{rabbit}(t)$ represents the position of the rabbit, $X_a(t)$ signifies the average position of the entire Harris hawks population, which can obtain using Equation (2), and r_1, r_2, r_3, r_4, and q are random numbers ranging from 0 to 1.

To minimize energy expenditure, Harris hawks adjust their behavior based on the prey's condition, making decisions between exploration and exploitation. The prey's condition is represented by its escape energy, as shown in Equation (3).

$$E_t = 2E_0\left(1 - \frac{t}{T}\right) \quad (3)$$

where E_t represents the escape energy of the prey at the t iteration, E_0 represents the initial escape energy, which is randomly sampled from the interval $[-1, 1]$, and T represents the maximum number of iterations.

During the exploitation phase, hawks make decisions among four attack strategies based on the prey's escape probability r and escape energy E_t.

(1) Soft besiege (see Figure 2a):

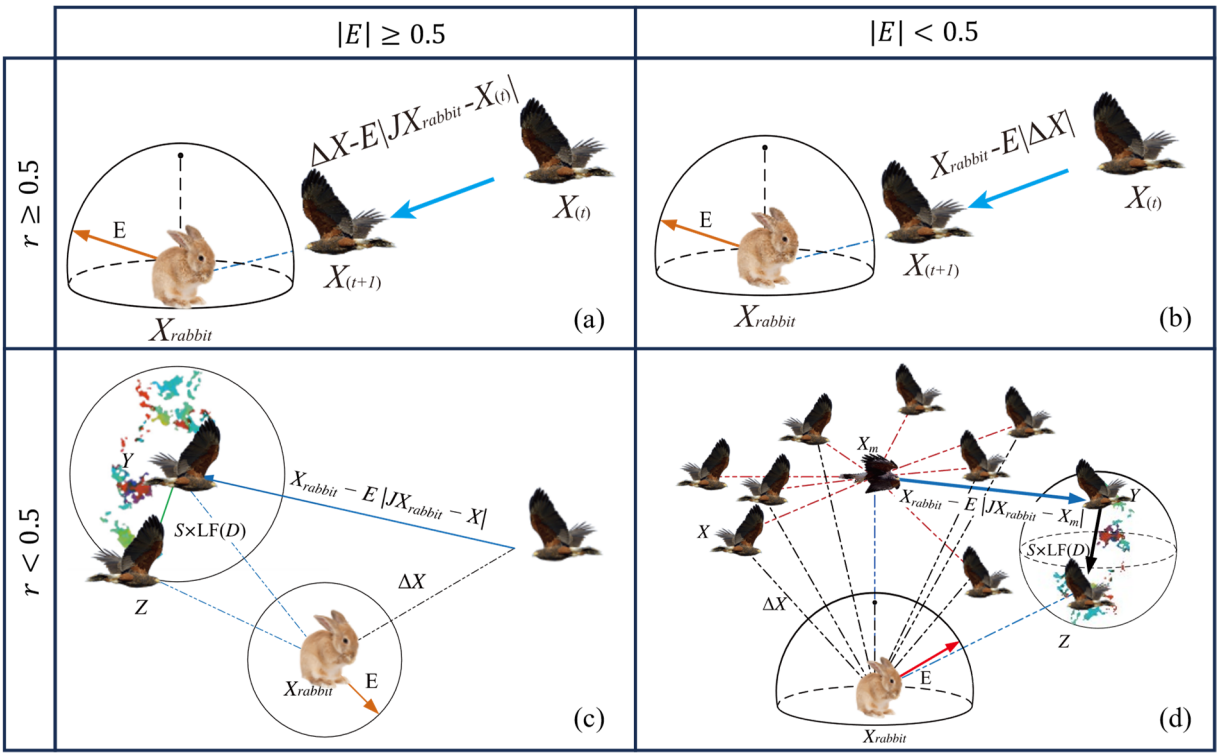

Figure 2. Four attack strategies of Harris hawks during exploitation phase: (**a**) soft besiege, (**b**) hard besiege, (**c**) soft besiege with progressive rapid dives, (**d**) hard besiege with progressive rapid dives.

While $r \geq 0.5$ and $|E_t| \geq 0.5$, the updating scheme for the Harris hawk's position is as follows in Equations (4)–(6):

$$X_i(t+1) = \Delta X_i(t) - E_t|JX_{rabbit}(t) - X_i(t)| \tag{4}$$

$$\Delta X_i(t) = X_{rabbit}(t) - X_i(t) \tag{5}$$

$$J = 2(1 - r_5) \tag{6}$$

where $\Delta X_i(t)$ represents the distance between the i hawk and rabbit at iteration t, J represents the random jumping strength during the rabbit's escape process, and r_5 is random numbers ranging from 0 to 1.

(2) Hard besiege (see Figure 2b):

While $r \geq 0.5$ and $|E_t| < 0.5$, the updating scheme for the Harris hawk's position is as in Equation (7):

$$X_i(t+1) = X_{rabbit}(t) - E_t|\Delta X_i(t)| \tag{7}$$

(3) Soft besiege with progressive rapid dives (see Figure 2c):

While $r < 0.5$ and $|E_t| \geq 0.5$, the updating scheme for the Harris hawk's position is as follows in Equations (8)–(10):

$$X_i(t+1) = \begin{cases} Y \; if \; F(Y) < F(X_i(t)) \\ Z \; if \; F(YZ) < F(X_i(t)) \end{cases} \tag{8}$$

$$Y = X_{rabbit}(t) - E_t|\Delta X_i(t)| \tag{9}$$

$$Z = Y + S \times LF(D) \tag{10}$$

where D represents the dimensionality of the optimization problem, S is a random vector of size $1 \times D$ dimensions, and LF represents the levy flight function [35].

(4) Hard besiege with progressive rapid dives (see Figure 2d):

While $r < 0.5$ and $|E_t| < 0.5$, the updating scheme for the Harris hawk's position is as follows in Equations (11)–(13):

$$X_i(t+1) = \begin{cases} Y \; if \; F(Y) < F(X_i(t)) \\ Z \; if \; F(YZ) < F(X_i(t)) \end{cases} \tag{11}$$

$$Y = X_{rabbit}(t) - E_t|JX_{rabbit}(t) - X_a(t)| \tag{12}$$

$$Z = Y + S \times LF(D) \tag{13}$$

The HHO algorithm can automatically adjust its trapping strategy during the iteration process; only two hyperparameters are required to set: the number of Harris hawks and the number of iterations. It exhibits strong search capabilities and convenience. Moreover, the search strategy is associated with the number of iterations, and the closer to the maximum number of iterations, the higher the possibility that the algorithm adopts an aggressive search strategy. This can well avoid the situation wherein the search result is a local optimum.

3. Strength Criteria

3.1. Principal Stress Space

The Cartesian coordinate system formed by the three principal stresses (maximum principal stress σ_1, intermediate principal stress σ_2, minimum principal stress σ_3) is referred to as the principal stress space, also known as the Haigh–Westergaard space [36]. The principal stress space is primarily utilized for depicting the geometric shapes of strength criteria, with specific parameters named as shown in Figure 3. Along the hydrostatic pressure axis, the three principal stresses are equal. The deviatoric plane (also referred to as the π-plane) is perpendicular to the hydrostatic pressure axis, where the sum of the three principal stresses at each point on it is a constant value denoted by I_1, which can be represented by Equation (14). I_1 is also known as the first stress invariant. In the figure, r represents the distance between point P and the hydrostatic axis, characterizing the magnitude of the shear stress. θ, also known as the Lode angle, ranges from 0° to 60° (some researchers use -30° to 30°). When $\theta = 0^\circ$, the relationship between the three principal stresses is $\sigma_1 > \sigma_2 = \sigma_3$, which is referred to as the triaxial compression meridian boundary (CMB). When $\theta = 60^\circ$, the relationship between the three principal stresses is $\sigma_1 = \sigma_2 > \sigma_3$, which is referred to as the triaxial tensile meridian boundary (TMB). Based on the relevant concepts of shear stress, the principal stress state, stress invariants, as well as parameters like θ and r can be interconnected. The specific transformation relationships are shown in the Equations (14)–(17):

$$I_1 = 3S_8 = \sigma_1 + \sigma_2 + \sigma_3 \tag{14}$$

$$r = \sqrt{2J_2} = \frac{\sqrt{3}}{3}T_8 = \sqrt{\frac{1}{3}\left[(\sigma_1 - \sigma_2)^2 + (\sigma_2 - \sigma_3)^2 + (\sigma_1 - \sigma_3)^2\right]} \tag{15}$$

$$\theta = \tan^{-1}\left(\sqrt{3}\frac{\sigma_2 - \sigma_3}{\sigma_1 - \sigma_3} \Big/ \left(2 - \frac{\sigma_2 - \sigma_3}{\sigma_1 - \sigma_3}\right)\right) \tag{16}$$

$$\begin{cases} \sigma_1 = \frac{\sqrt{6}}{3} r\cos\theta \\ \sigma_2 = \frac{\sqrt{6}}{3} r\cos\left(\frac{2\pi}{3} - \theta\right) \\ \sigma_3 = \frac{\sqrt{6}}{3} r\cos\left(\frac{2\pi}{3} + \theta\right) \end{cases} \tag{17}$$

where S_8 denotes the octahedral normal stress, J_2 denotes the second bias stress invariant, and T_8 denotes the octahedral shear stress.

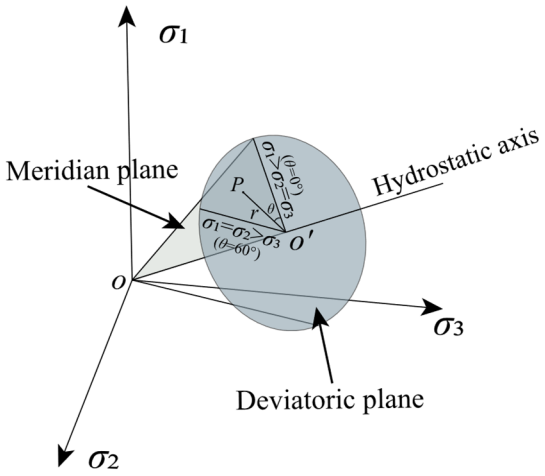

Figure 3. Schematic description of the strength criteria in the principal stress space.

3.2. DP Criterion

The DP criterion is the most commonly used strength criterion in wellbore stability analysis. It was proposed by Drucker and Prager [14] by extending the Von Mises criterion. The specific form of the DP criterion is as in Equation (18):

$$\sqrt{J_2} - aI_1 - k = 0 \tag{18}$$

where a and k are material constants, which relate to the internal friction angle φ and the cohesion c. a and k can be determined using the following Equations (19) and (20):

$$a = \frac{2\sin\varphi}{\sqrt{3}(3 \mp \sin\varphi)} \tag{19}$$

$$k = \frac{6c\cos\varphi}{\sqrt{3}(3 \mp \sin\varphi)} \tag{20}$$

3.3. HB Criterion

The HB criterion, developed by Hoek et al. [7] through fitting true triaxial test data, is an empirical criterion widely used in the field of geotechnical engineering. Among various criteria in geotechnical engineering, the HB criterion stands out as one of the most extensively applied. Its specific form is as in Equation (21):

$$\sigma_1 = \sigma_3 + \sigma_c\left(m\frac{\sigma_3}{\sigma_c} + 1\right)^{0.5} \tag{21}$$

where m is a constant associated with the rock type. For intact sandstone, the range of m typically falls between 13 and 21 [37].

3.4. MGC Criterion

Al-Ajmi and Zimmerman, through analysis of rock true triaxial test data, observed a clear linear relationship between the octahedral shear stress and the mean effective stress of the rock. Based on this observation, they proposed a linear Mogi criterion, which is similar to the Mohr–Coulomb criterion and, hence, referred to as the MGC criterion [21]. The specific equations for the MGC are as in Equations (22)–(27):

$$\tau_{oct} = a + b\sigma_{m,2} \tag{22}$$

where

$$\tau_{oct} = \frac{1}{3}\sqrt{(\sigma_1 - \sigma_2)^2 + (\sigma_2 - \sigma_3)^2 + (\sigma_1 - \sigma_3)^2} \tag{23}$$

$$\sigma_{m,2} = \frac{\sigma_1 + \sigma_3}{2} \tag{24}$$

$$a = \frac{2\sqrt{2}}{3}\frac{\sigma_c}{k+1} \tag{25}$$

$$b = \frac{2\sqrt{2}}{3}\frac{k-1}{k+1} \tag{26}$$

$$k = \frac{1+\sin\varphi}{1-\sin\varphi} \tag{27}$$

3.5. ML Criterion

The Lade–Duncan criterion [16] is a strength criterion originally developed for cohesionless soils. To extend its application to rock materials, Ewy improved upon it, resulting in the ML criterion. The specific form of the ML criterion is as in Equations (28)–(32):

$$\frac{L_1^3}{L_3} = \left(3^3 + \eta\right) \tag{28}$$

$$L_1 = (\sigma_1 + S) + (\sigma_2 + S) + (\sigma_3 + S) \tag{29}$$

$$L_3 = (\sigma_1 + S)(\sigma_2 + S)(\sigma_3 + S) \tag{30}$$

where S and η are coefficients related to the rock cohesion c and the angle of internal friction φ, respectively.

$$S = \frac{c}{tan\varphi} \tag{31}$$

$$\eta = \frac{4tan^2\phi(9 - 7sin\varphi)}{1 - sin\varphi} \tag{32}$$

3.6. MWC Criterion

The MWC criterion [17] is an extension of the DP criterion based on Griffith microcracking theory. Due to its similarity in form to the Weibols–Cook criterion, it is referred to as MWC. The specific form for MWC is as in the following equations:

$$J_2^{\frac{1}{2}} = A + BJ_1 + CJ_1^2 \tag{33}$$

$$J_1 = \frac{\sigma_1 + \sigma_2 + \sigma_3}{3} \tag{34}$$

$$J_2^{\frac{1}{2}} = \sqrt{\frac{1}{6}\left[(\sigma_1 - \sigma_2)^2 - (\sigma_2 - \sigma_3)^2 + (\sigma_3 - \sigma_1)^2\right]} \tag{35}$$

$$C = \frac{\sqrt{27}}{2C_1 + (q-1)\sigma_3 - \sigma_c}\left[\frac{C_1 + (q-1)\sigma_3 - \sigma_c}{2C_1 + (2q+1)\sigma_3 - \sigma_c} - \frac{q-1}{q+2}\right] \tag{36}$$

$$C_1 = (1 + 0.6c)\sigma_c \tag{37}$$

$$q = \tan\left(\frac{\pi}{4} + \frac{\varphi}{2}\right)^2 \tag{38}$$

$$B = \frac{\sqrt{3}(q-1)}{q+2} - \frac{C}{3}[2C_0 + (q+2)\sigma_3] \tag{39}$$

$$A = \frac{\sigma_c}{\sqrt{3}} - \frac{\sigma_c}{3}B - \frac{\sigma_c^2}{3}C \tag{40}$$

4. Data Description

Fourteen different sandstone true triaxial datasets were collected from existing studies, encompassing uniaxial compressive strength (UCS, σ_c) and the maximum principal stresses (σ_1), intermediate principal stresses (σ_2), and minimum principal stresses (σ_3) at failure. The characteristics of these datasets, along with their references, are presented in Table 1. To facilitate model training and evaluation, the collected data were randomly divided into a training set (70%) and testing set (30%). Figure 4 illustrates the correlations between the collected variables and the distributions of the training and testing sets. It can be observed from the figure that the distributions of the training and testing sets are highly consistent, and the correlations between variables within each dataset are also similar.

Table 1. Statistical description of variables in the datasets.

Number	Number of Data	σ_1 (MPa)		σ_2 (MPa)		σ_3 (MPa)		References
		Min	Max	Min	Max	Min	Max	
1	29	92.1	492.1	10	413	10	100	[38]
2	17	87.48	302.8	0	62.5	0	37.5	[39]
3	23	25.91	172	0	60	0	20	[40]
4	24	34.62	128.68	0	24	0	10	[41]
5	44	74.22	279	0	171	0	50	[42]
6	20	75.4	194	0	118.3	0	15	[42]
7	14	48.5	159.1	0	24	0	6.6	[43]
8	14	49.4	165.9	0	24	0	6.6	[43]
9	14	46.4	147.6	0	24	0	6.6	[43]
10	31	60	465	0	436	0	50	[44]
11	27	184.17	378.68	0	160	0	10	[45]
12	20	23.69	192.97	0	55.2	0	55.2	[46]
13	78	56.1	648	0	620.7	0	150	[47]
14	62	29.7	370.2	0	346.3	0	150	[47]

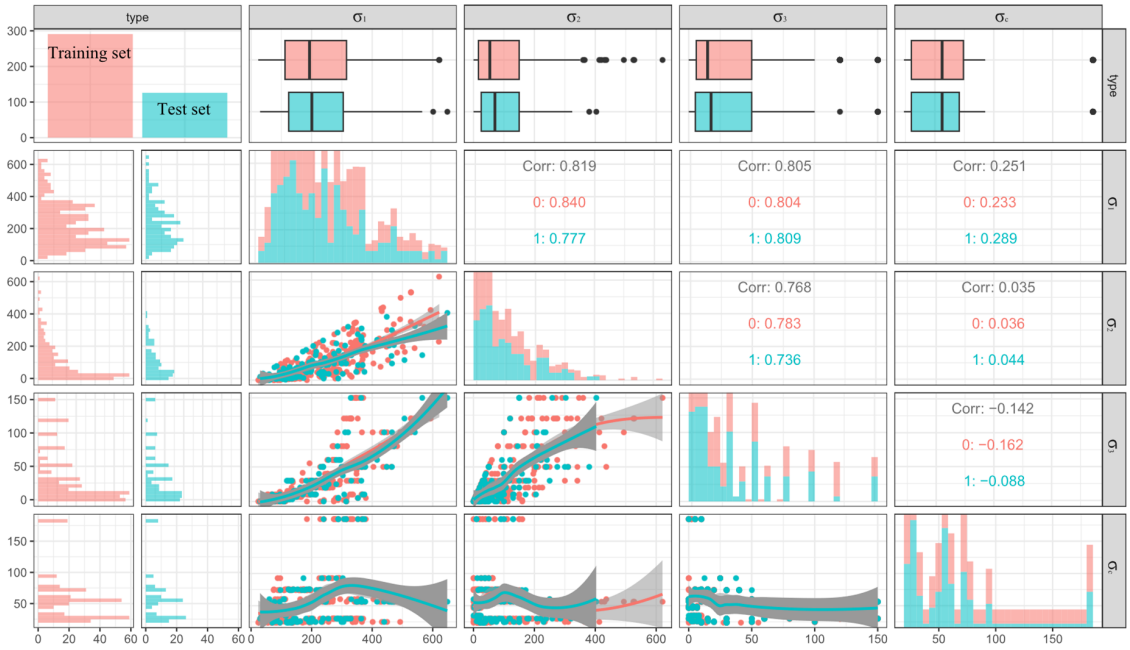

Figure 4. Correlations between input and output variables.

Figure 5 illustrates the distribution of θ obtained from the collected true triaxial experimental data. It is evident from the figure that most experiments do not cover the entire range of θ, which fails to reflect the variation in the true triaxial strength of rocks as the stress conditions transition from CBM to TBM. When utilizing such data for model

training, it becomes challenging for the model to accurately assess the unexplored range of θ. Hence, during the model training process, it was essential to uniformly input experimental data from different sandstones into the model to ensure the accurate prediction of the true triaxial strength of rocks across the entire range of θ. Additionally, the data obtained for sandstone No. 10 cover a relatively complete range of θ compared to other sandstones. Moreover, the trend of the true triaxial strength of the rock when the stress condition changes from CBM to TBM for similar I_1 states is also presented more clearly. Therefore, for subsequent analyses of the deviatoric plane and failure envelope shape, sandstone No. 10 was selected as a comparative reference.

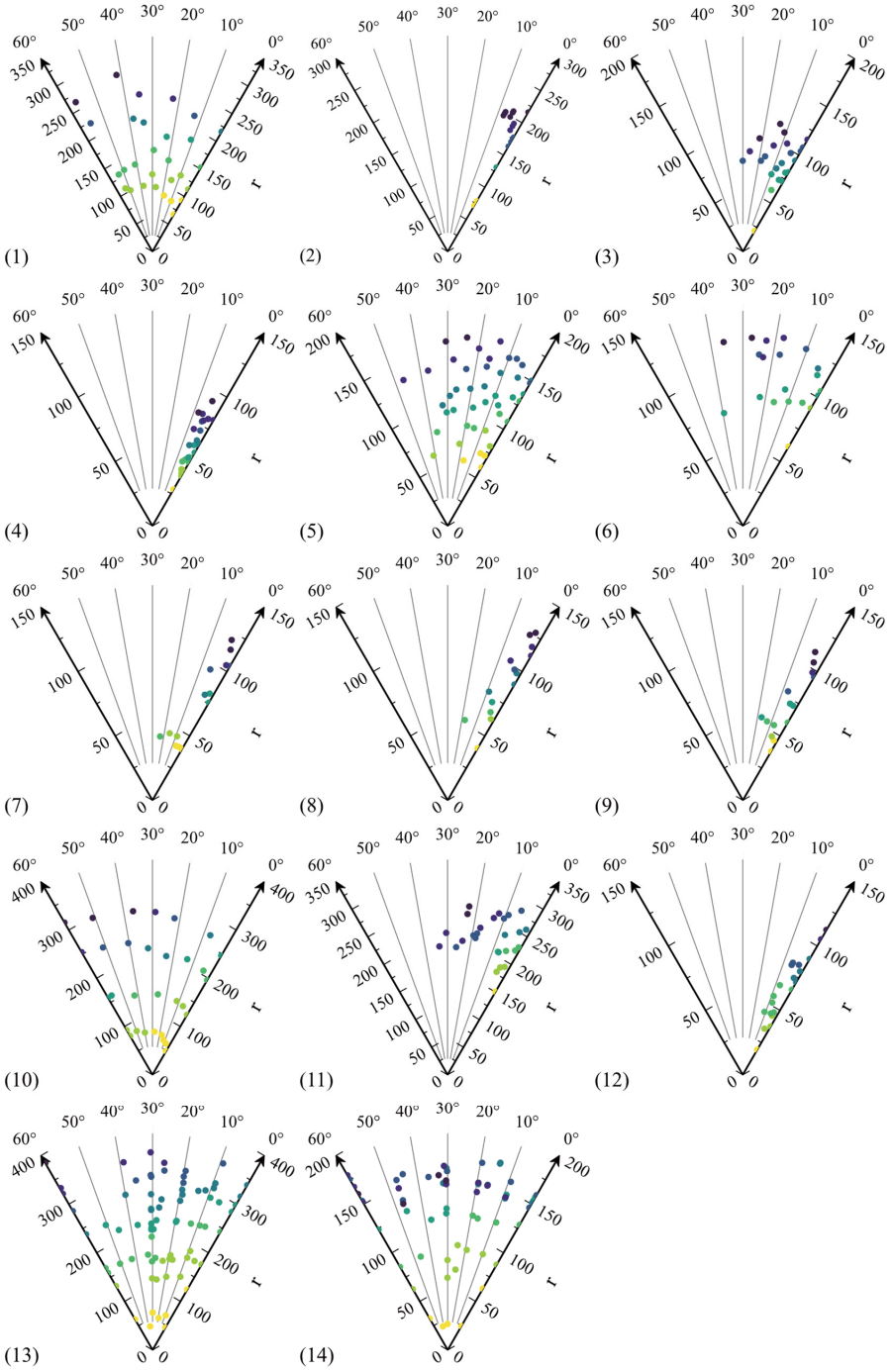

Figure 5. The θ distributions of true triaxial data for different sandstones.

5. Model Building and Training

The settings of hyperparameters in the MLP model significantly influence its performance. Reasonable hyperparameter settings enable the MLP model to adapt to the training data more accurately during the training process. HHO, as a multi-strategy optimization algorithm, can adjust its optimization strategies based on the remaining number of iterations, effectively preventing the model from becoming prematurely trapped in local optima. HHO has already been proven in numerous studies to be a highly effective method for hyperparameter optimization [48–50]. In this study, the HHO was chosen as the optimization method for finding suitable hyperparameter settings for the MLP model. To effectively establish and evaluate the HHO-MLP model, the sandstone database was randomly divided into training and testing datasets in a 7:3 ratio.

Considering that in numerical analysis, models need to be converted into explicit expressions for further operations, the complexity of the explicit expressions of model outputs should be minimized to improve the convenience of further applications. Therefore, the number of hidden layers in the model was set to one, and the activation function of the output layer was set to linear. Additionally, to ensure the differentiability of the expressions, continuous and differentiable functions were selected as activation functions for the hidden layer. Through analysis of existing activation functions, four activation functions were selected for model establishment. Table 2 shows the specific forms of the activation functions.

Table 2. Expressions for four activation functions.

Name	Equation
sigmoid	$sigmiod(x) = \frac{1}{1+e^{-x}}$
softplus	$softplus(x) = \log(1 + e^{x})$
swish	$swish(x) = x \times sigmoid(\beta\ ^{1} \times x)$
tanh	$tanh(x) = \frac{e^{x}-e^{-x}}{e^{x}+e^{-x}}$

[1] β: trainable variable.

During the model training process, the parameters for the optimizer HHO were 20 for the number of Harris hawks and 50 for the number of iterations. The hyperparameters optimized include the batch size, the number of nodes per layer, and the learning rate of the MLP model. These parameters were set within specific ranges during the optimization process (batch size [1, 50], number of nodes per layer [1, 100], learning rate [1×10^{-6}, 1×10^{-3}]). Additionally, to enhance the model's generalization performance, 20% of the training set was allocated as a validation set to evaluate the model's performance during training. The Mean Squared Error (MSE) was selected as the fitness function to assess the model's fitness, which can be calculated by Equation (41).

$$MSE = \frac{\sum_{i=1}^{n}(f_i - y_i)^2}{n} \tag{41}$$

where f_i denotes the predicted value and y_i, denotes the actual value.

The iteration process for the models employing four different activation functions is depicted in Figure 6. From the figure, it is evident that HHO significantly optimizes all four MLP models. Most models exhibit convergence of MSE within 30 iterations, with complete convergence observed after 40 iterations. In terms of training results, the model using tanh as the activation function performed the best among the four, followed by sigmoid, softplus, and swish. Following the conventional pattern for selecting ML models, it is apparent that the model with tanh activation function would be chosen for further research. However, as mentioned earlier, the shape of the envelope corresponding to the rock strength model is also a crucial indicator of model performance. Therefore, further comparison of the four models obtained was necessary.

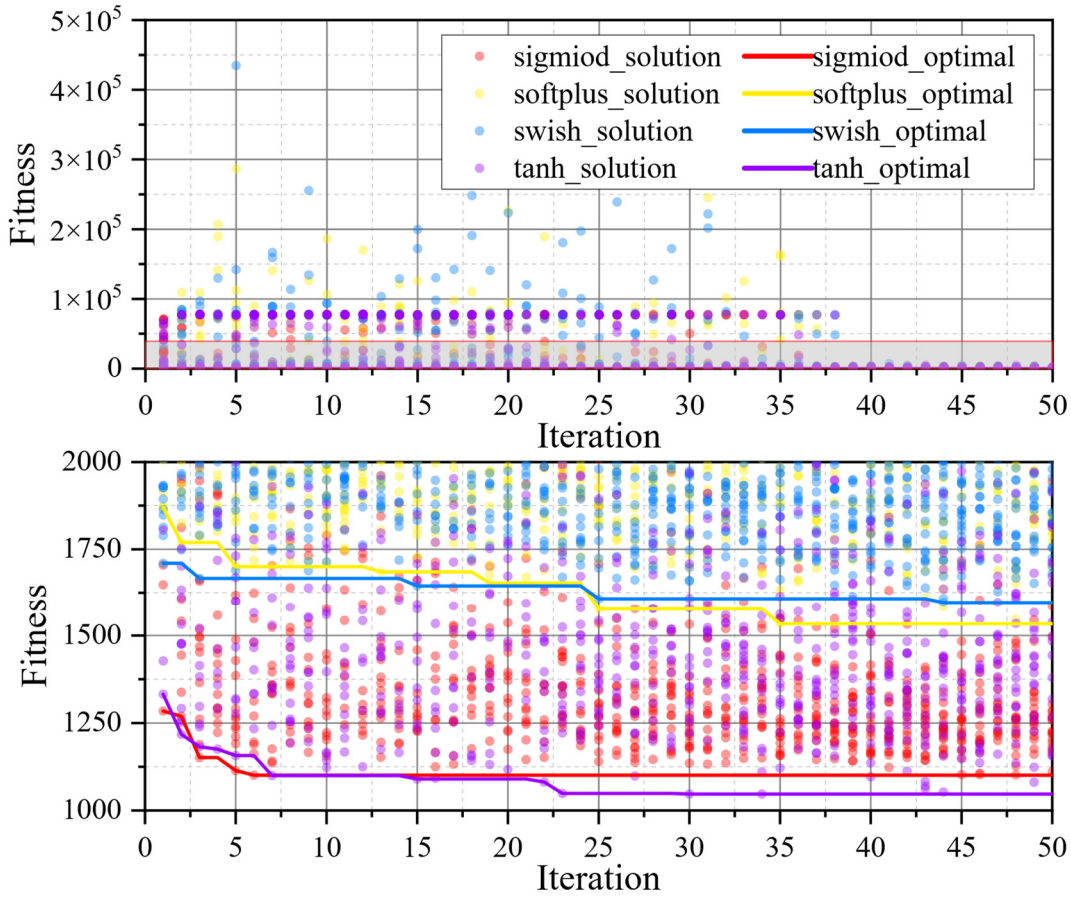

Figure 6. Optimization iteration process of HHO-MLP model utilizing different activation functions.

Figure 7 illustrates the compressive and tensile meridians obtained by the four models when predicting the behavior of sandstone No. 10. It is evident from the figure that all four models demonstrate excellent predictive capabilities around the data points. However, it can be observed from the figure that the model with the sigmoid activation function erroneously predicts the tensile meridian behavior of the sandstone No. 10 under low S_8 conditions and the compressive meridian behavior of the rock under high S_8 conditions. Similarly, the model using tanh as the activation function incorrectly predicts the compressive meridian behavior of the rock under high S_8 conditions. In contrast, the compressive and tensile meridians presented by the models using softplus and swish as activation functions are more consistent with the widely accepted pattern of rock compressive and tensile meridians. Considering the final fitness of the models, the model using softplus as the activation function outperforms the model using swish as the activation function. Furthermore, in terms of the fit between the compressive and tensile meridians and experimental data, the model with softplus as the activation function also outperforms the model with swish as the activation function. Therefore, the model with softplus as the activation function was selected as the final model for comparison with traditional strength criteria. The parameters of the MLP model with softplus as the activation function finally obtained by HHO were set (batch size: 2, number of nodes per layer: 98, learning rate: 0.981×10^{-3}). Equation (42) represents the final obtained HHO-MLP model.

$$\sigma_1 = \left| \log\left(1 + e^{W^{[1]}A^{[0]}+B^{[1]}}\right) W^{[2]} + B^{[2]} \right| \tag{42}$$

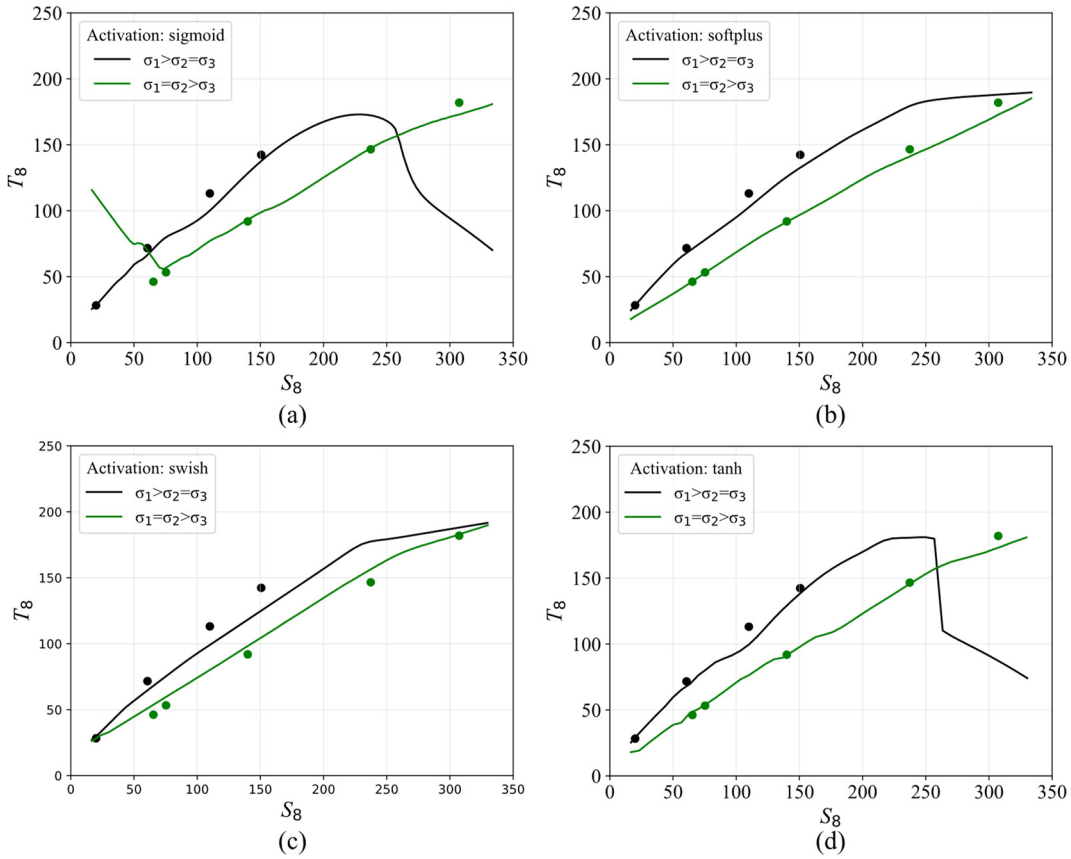

Figure 7. Performance of HHO-MLP models utilizing different activation functions in the meridian plane: (**a**) sigmoid, (**b**) softplus, (**c**) swish, (**d**) tanh.

6. Performance Comparison

6.1. Comparisons Using the Collection Dataset

In order to evaluate the performance of the obtained model, we compared the HHO-MLP model with five existing rock strength criteria (DP, HB, MGC, ML, and MWC) on both the training and testing datasets, considering that these five strength criteria each involve parameters related to rock properties such as cohesion and friction angle, and that such parameters are not explicitly provided in the literature from which the dataset originated. To ensure a fair comparison of model performance, the parameters of the various strength criteria were fitted using the data from the training set through the least squares method, following the methodology outlined by Rukhaiyar et al. [27] and Zhou et al. [25]. The parameter settings obtained for the five different rock types through fitting are presented in Table 3.

The obtained HHO-MLP model and the five strength criteria were used to predict the training set data and test set data. Figure 8 shows the comparison between the actual values and the predicted values obtained from the HHO-MLP model and the five strength criteria. From Figure 8, it can be seen that the scatter plots of the HHO-MLP model are closely surrounding the Y = X line in both the training and test sets, and the upper and right distributions are similar in shape. The scatter plots of the remaining five strength criterion models show large dispersion, especially for σ_1 > 400 Mpa. This demonstrates the strong generalization ability and good prediction accuracy of HHO-MLP for various sandstone types as well as stress conditions. The traditional strength criteria have inapplicable rock types and stress conditions with poor generalization performance. Furthermore, the figure illustrates that the predicted values remain constant across different intermediate principal stress conditions due to the Hoek–Brown criterion's failure to incorporate the influence of intermediate principal stresses.

Table 3. Parameter sets of different strength criteria for different sandstones.

Sandstone Number	DP		HB	MGC	ML			MWC
	a	*k*	*m*	*k*	*S*	*η*	*q*	*c* (MPa)
1	0.17	33.87	21	3.9	21.3	13.71	2.84	7.6
2	0.33	25.04	21	5.87	17.38	45.7	4.77	1.37
3	0.32	13.73	21	8.96	12.16	54.21	0.64	0.73
4	0.37	7.25	21	7.13	10.29	60.11	6.19	1255.77
5	0.21	28.3	13.86	3.62	19.29	17.18	3.09	0.14
6	0.16	38.4	18.68	4.19	20	18.93	3.89	0.26
7	0.46	1.78	21	12.04	6.67	184.7	9.29	0.63
8	0.45	6.27	21	14.07	8.31	169.15	10.65	4.91
9	0.43	4.58	21	10.56	7.86	138.2	8.28	0.89
10	0.23	31.92	21	6.02	17.54	37	4.41	2.23
11	0.18	92.66	21	6.56	33.79	31.26	6.21	0.66
12	0.24	9.72	15.01	3.49	13.54	16.12	0.43	0.97
13	0.17	53.62	21	3.8	29.63	11.44	1.04	1.87
14	0.1	43.29	13	2.43	26.56	1.68	0.73	3.6

To quantitatively compare the performance of the six strength models, four commonly used evaluation metrics were selected to assess the models' predictive performance. These evaluation metrics are R^2 (Coefficient of Determination), MAE (Mean Absolute Error), RMSE (Root Mean Square Error), and MAPE (Mean Absolute Percentage Error). The R^2 was used to evaluate the degree of agreement between predicted values and actual values in regression models [51–53], and it can be calculated using Equation (43).

$$R^2 = \frac{\sum_{i=1}^{n}(\overline{y} - f_i)^2}{\sum_{i=1}^{n}(y_i - \overline{y})^2} \tag{43}$$

where $\overline{y}$ denotes the mean of the actual values.

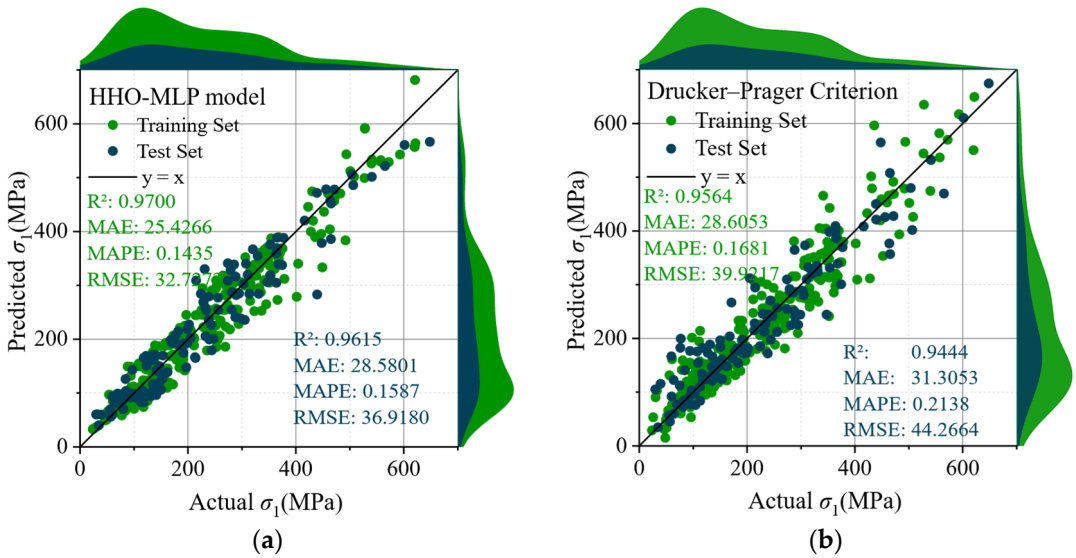

Figure 8. *Cont.*

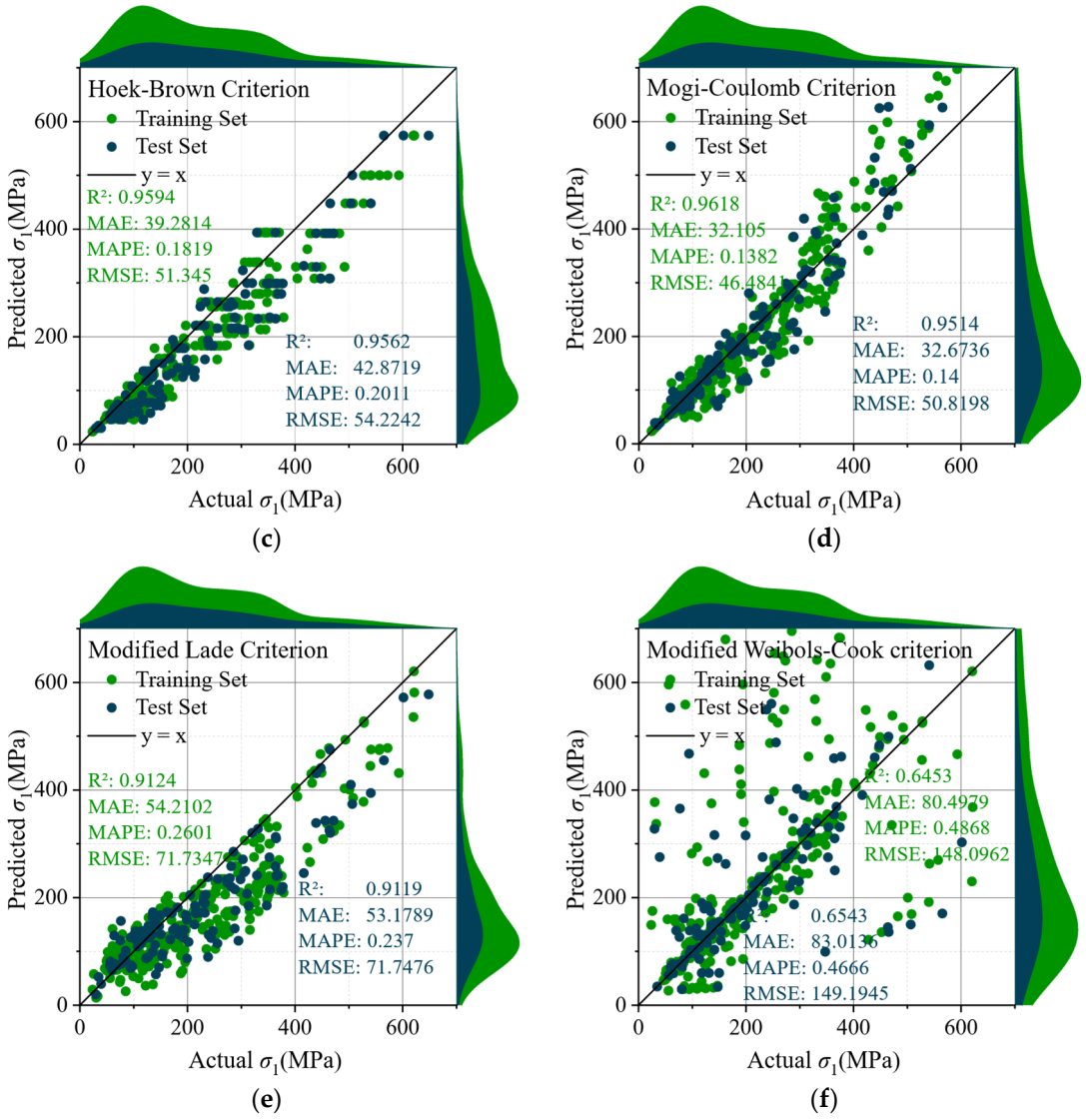

Figure 8. Scatter plots of actual and predicted values of σ_1 for training and testing datasets: (**a**) HHO-MLP model, (**b**) DP criterion, (**c**) HB criterion, (**d**) MGC criterion, (**e**) ML criterion, (**f**) MWC criterion.

The MAE accurately reflects the magnitude of errors between predicted values and actual values [54], and it can be calculated using Equation (44).

$$MAE = \frac{1}{n}\sum_{i=0}^{n}|f_i - y_i| \tag{44}$$

RMSE denotes the standard deviation of the fitting error between the predicted and actual values, and it can be calculated using Equation (45).

$$RMSE = \sqrt{\frac{\sum_{i=1}^{n}(f_i - y_i)^2}{n}} \tag{45}$$

The MAPE represents the proportion of errors between predicted values and actual values relative to the actual values, and it can be calculated using Equation (46).

$$MAPE = \frac{1}{n}\sum_{i=0}^{n}\left|\frac{f_i - y_i}{y_i}\right| \tag{46}$$

Table 4 presents an overview of the evaluation metrics for the predictions made by the six strength models. It is evident from the table that the HHO-MLP model marginally underperforms the MGC concerning MAPE in the training set evaluation (HHO-MLP: 0.1435, MGC: 0.1382). However, it notably outperforms the five strength criteria in terms of R^2 (0.9700), MAE (25.4266), and RMSE (32.7273). Similarly, in the test set performance, the HHO-MLP model exhibits a slight underperformance compared to the MGC in MAPE (HHO-MLP: 0.1587, MGC: 0.14), while still significantly surpassing its five strength criterion counterparts in R^2 (0.967), MAE (26.3836), and RMSE (34.1815). Additionally, the proximity of the evaluation metrics values between the training and test sets for the HHO-MLP model further underscores its remarkable generalization performance.

Table 4. Prediction performance evaluation metrics of 6 strength models in training and test sets.

Model	Training				Test			
	R^2	MAE	RMSE	MAPE	R^2	MAE	RMSE	MAPE
HHO-MLP	0.9700	25.4266	32.7273	0.1435	0.9615	28.5801	36.9180	0.1587
DP	0.9564	28.6053	39.9217	0.1681	0.9444	31.3053	44.2664	0.2138
HB	0.9594	39.2814	51.345	0.1819	0.9562	42.8719	54.2242	0.2011
MGC	0.9618	32.105	46.4841	0.1382	0.9514	32.6736	50.8198	0.14
ML	0.9124	54.2102	71.7347	0.2601	0.9119	53.1789	71.7476	0.237
MWC	0.6453	80.4979	148.0962	0.4868	0.6543	83.0136	149.1945	0.4666

Taylor diagrams, renowned for their comprehensive and intuitive depiction of model performance, have emerged as a favored method for model comparison and have been embraced by numerous researchers [55]. These diagrams enable the presentation of three distinct evaluation metrics (standard deviation, R^2, and RMSE) for models, effectively visualizing performance disparities between different models through the spatial representation of predicted and measurement points. Figure 9 depicts the performance of the six models on both the training and test sets. Upon examination of the figure, it becomes evident that the HHO-MLP model outperforms the five strength criterion models across both the training and test sets.

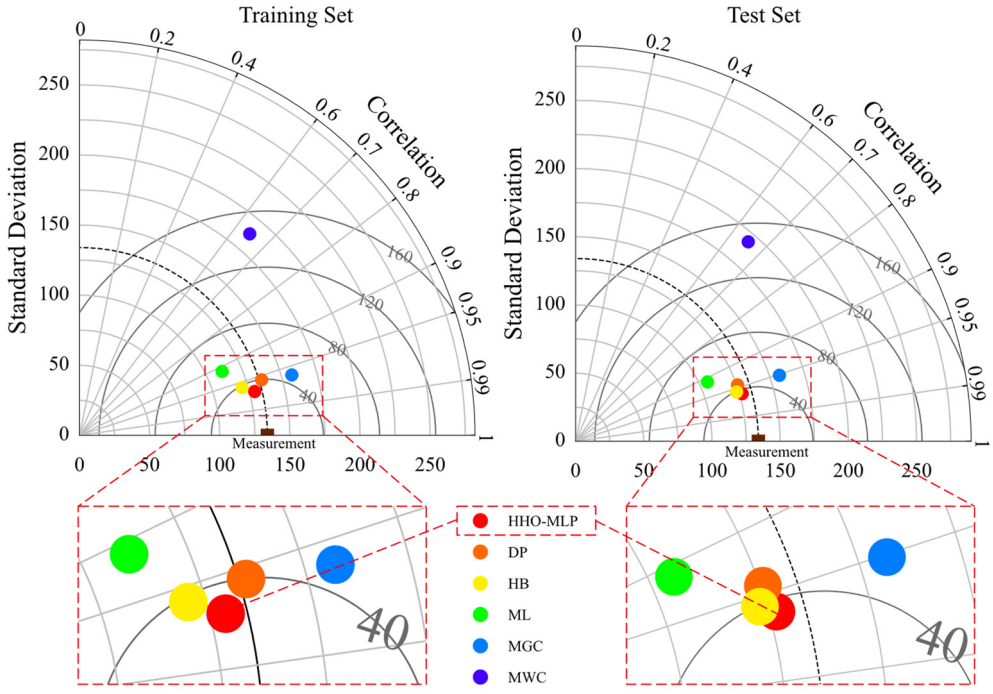

Figure 9. Taylor diagrams of 6 strength models.

6.2. Comparison on the Meridian Plane

Based on the analysis of scatter plots, tables, and Taylor diagrams, it is evident that the HHO-MLP model exhibits remarkable superiority over the collected dataset in comparison to the five strength criteria. However, comparing model performance solely on the collected dataset is not comprehensive. In Section 5, instances were noted where models performed well on the dataset but exhibited significant deviations from theoretical trends. Moreover, the distribution of sample points in Figure 5 shows that most of the experiments did not involve the region neighboring $\theta = 60^{\circ}$, while the overall amount of data is relatively small. Therefore, it is uncertain whether the model can completely describe the strength behavior of sandstone under different true triaxial stress states based only on the model's predicted performance on the dataset. To provide a more comprehensive analysis of model performance, it is necessary to explore the complete failure envelope of the models in the principal stress space. The shape of the failure envelope presented by the strength model is also a crucial characterization of strength model performance. Strength models need to satisfy criteria such as continuity, smoothness, differentiability, and convexity to be applicable for numerical analysis. Consequently, further investigation into the shape of the envelope of the model in the meridional plane, deviatoric plane, and in three dimensions is warranted.

Figure 10 shows the compressive and tensile meridians of No. 10 sandstone predicted by both the HHO-MLP model and the five strength criteria. Among the six strength models, only the compressive and tensile meridians predicted by the DP criterion notably deviate from the actual data points, whereas those predicted by the other five models exhibit better alignment with the actual data. Notably, the shape of the compressive and tensile meridians is predicted by the HHO-MLP model, which comprises two upwardly convex curves. Additionally, as the level of S_8 increases, the disparity between the T_8 values under the two conditions diminishes. The former characteristic of the tension–compression meridians predicted by the HHO-MLP model bears a resemblance to the HB criterion, which is an empirical strength criterion derived from fitting experimental data. The latter characteristic suggests that with an increase in I_1, significant changes will occur in the shape of the failure envelope of the HHO-MLP model on the deviatoric plane, aligning with the theoretical development trend of the failure envelope.

6.3. Comparison on the Deviatoric Plane

Since there are no experimental data available with the same I_1 for testing the specific performance of the models on the deviatoric plane, only the shapes of the models on the deviatoric plane are explored. Figure 11 illustrates the failure envelopes of the six models on the deviatoric plane for different I_1 conditions under the rock parameter condition of No. 10 sandstone. It can be observed from the figure that at $I_1 = 250$, the shape of the HHO-MLP model on the deviatoric plane resembles a straight line, akin to the shape and trend of the HB. At $I_1 = 500$, the shape of the HHO-MLP model on the deviatoric plane transforms into a curve, which exhibits a similar overall form and trend to the ML. At $I_1 = 750$, the shape change of the HHO-MLP model on the deviatoric plane becomes curved and the overall trend remains similar to that of the ML. At $I_1 = 1000$, the shape of the HHO-MLP model on the deviatoric plane closely resembles an arc, mirroring the shape and trend of the DP.

In contrast, the shapes of the deviatoric plane curves of the five strength criterion models change less with I_1. However, it is noteworthy that the curves of the HHO-MLP model on the deviatoric plane all exhibit slight undulations, unlike the remaining five strength criterion models, which do not display this phenomenon. This variation arises from the fact that the HHO-MLP model is trained using actual true triaxial test data. Natural rocks are inherently anisotropic, and even neighboring regions exhibit internal differences. Consequently, the mechanical property trends of different rocks within the same batch of tests may deviate from theoretical expectations. Most traditional strength criteria are developed based on various isotropic theories. Overall, the HHO-MLP model

demonstrates shapes similar to the different strength models in different deviatoric planes at different I_1 levels, and all satisfy the requirements of continuity and smoothness.

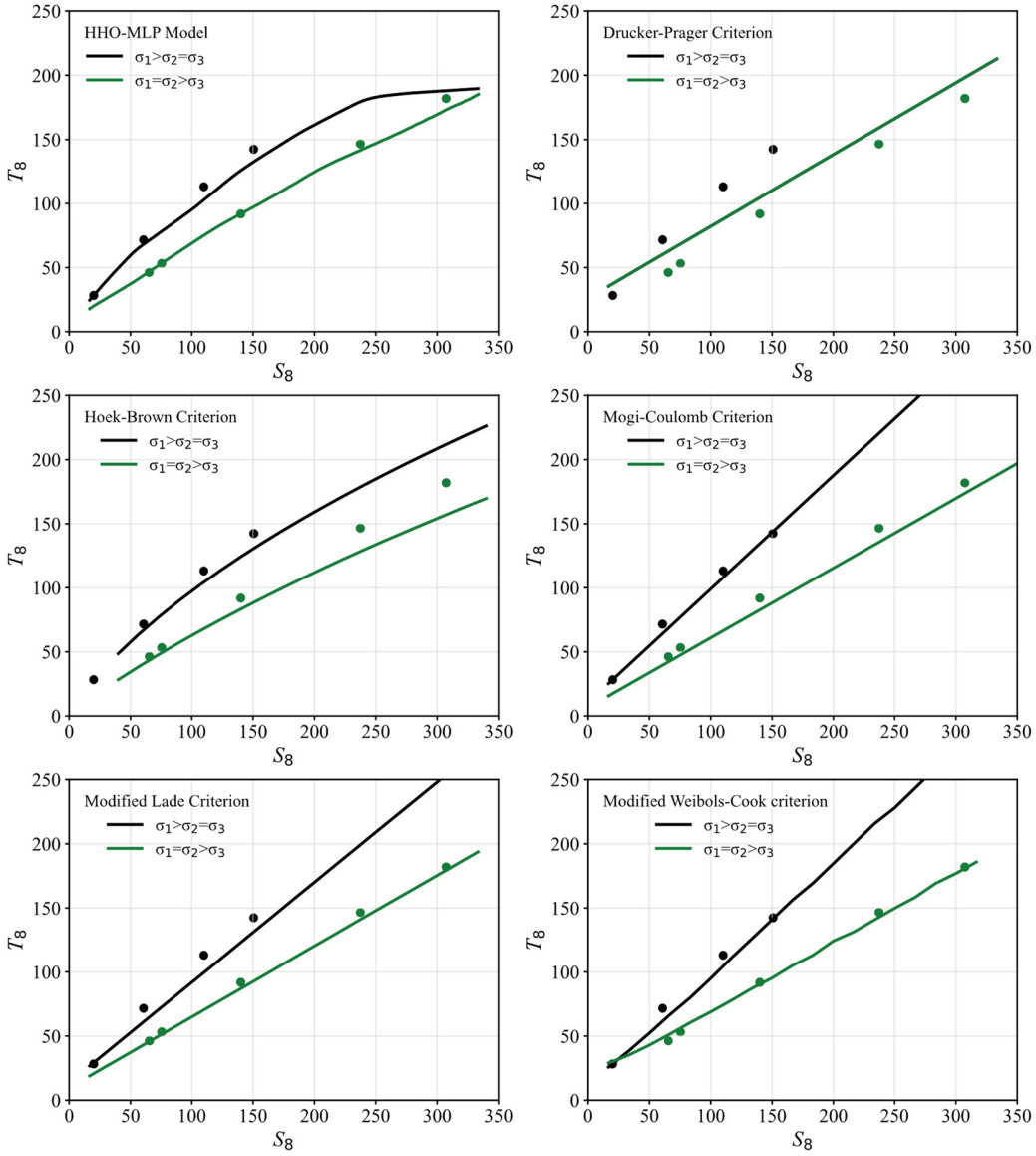

Figure 10. Performance of six strength models in the meridian plane.

6.4. Comparison on 3D Failure Envelope

Figure 12 presents the shapes of the failure envelopes and the variation in the $\frac{\sigma_1}{I_1}$, $\frac{\sigma_2}{I_1}$, and $\frac{\sigma_3}{I_1}$ on the deviatoric plane under the parameter conditions of No. 10 sandstone for the six models. The data points in the graph represent actual data points of No. 10 sandstone, with red indicating points within the envelope surface, implying overestimation of rock strength by the model, and green indicating points outside the envelope surface, indicating underestimation of rock strength by the model. From Figure 12a, it can be observed that for the HHO-MLP model, only three data points are in the red state, and they occur at lower stress states. This suggests that the HHO-MLP model predicts the strength of No. 10 sandstone conservatively. Moreover, the shape of the failure envelope is continuous, but with slight roughness and some lack of smoothness at the CMB and TMB. Among the failure envelopes of the six models, the DP and ML models exhibit good performance in terms of smoothness and continuity. However, in terms of differences from the actual data points, the DP model's predictions for actual data in small θ ranges are conservative, while

they are aggressive for data in large θ ranges. The ML model tends to overestimate rock strength under both small and large I_1 states. As for the HB model, its estimation of true triaxial strength remains conservative due to the neglect of the influence of intermediate principal stress. The MGC and MWC models show no significant regularity in predicting true triaxial strength.

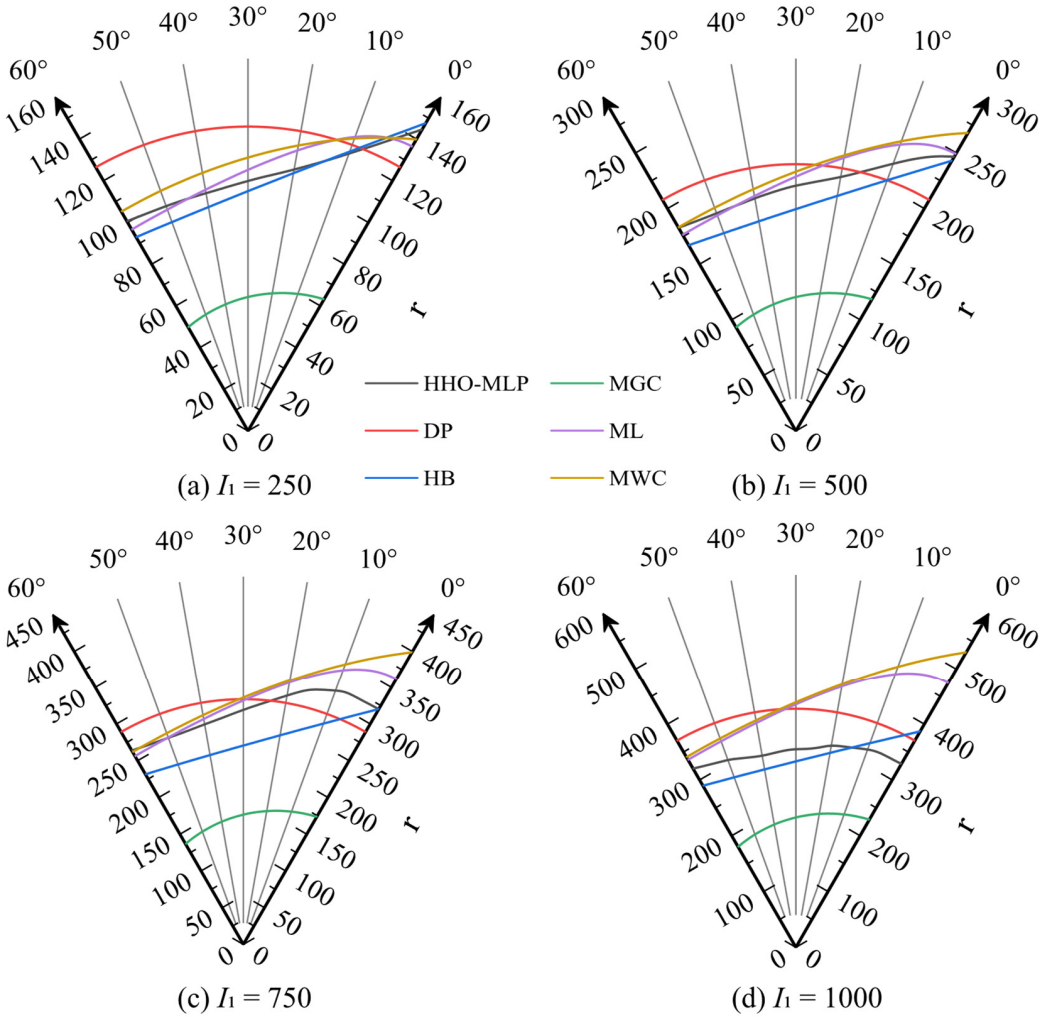

Figure 11. Shapes of the six strength models in the deviatoric plane for different I_1 conditions.

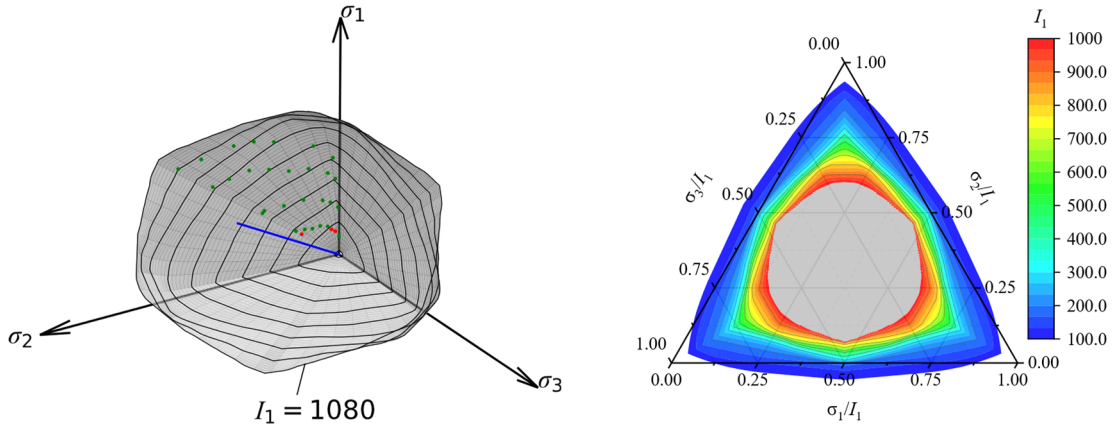

(**a**) HHO-MLP (**b**) HHO-MLP

Figure 12. *Cont.*

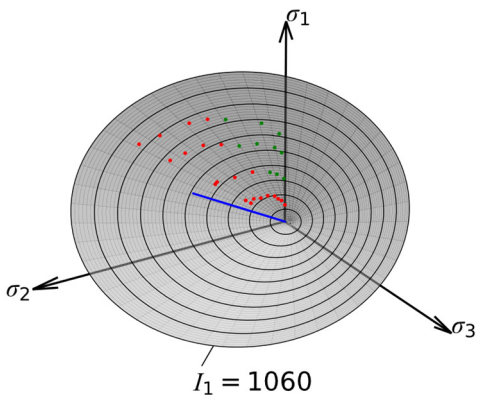

(**c**) DP

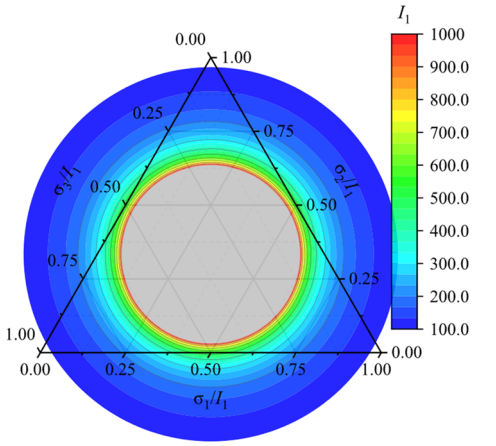

(**d**) DP

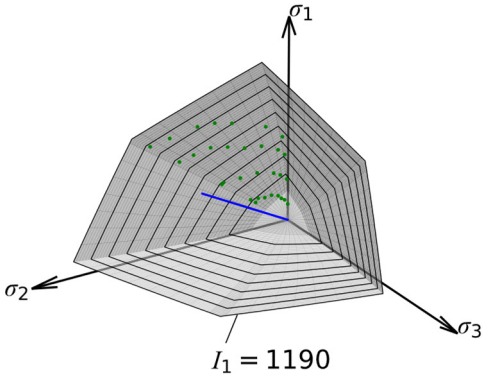

(**e**) HB

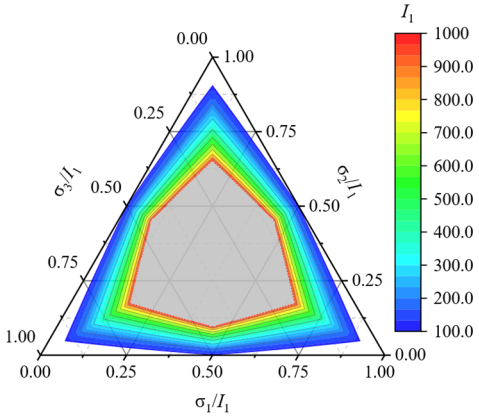

(**f**) HB

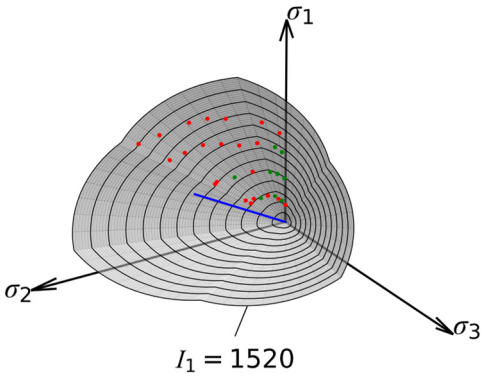

(**g**) MGC

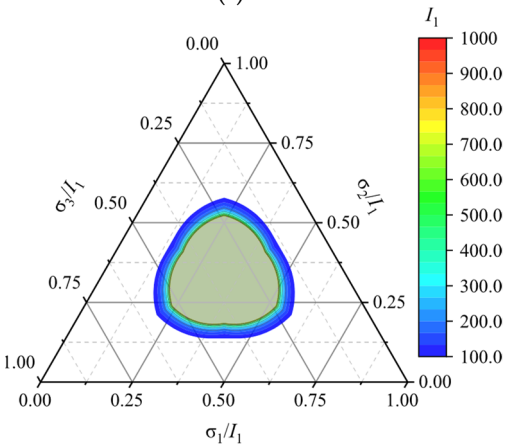

(**h**) MGC

Figure 12. *Cont.*

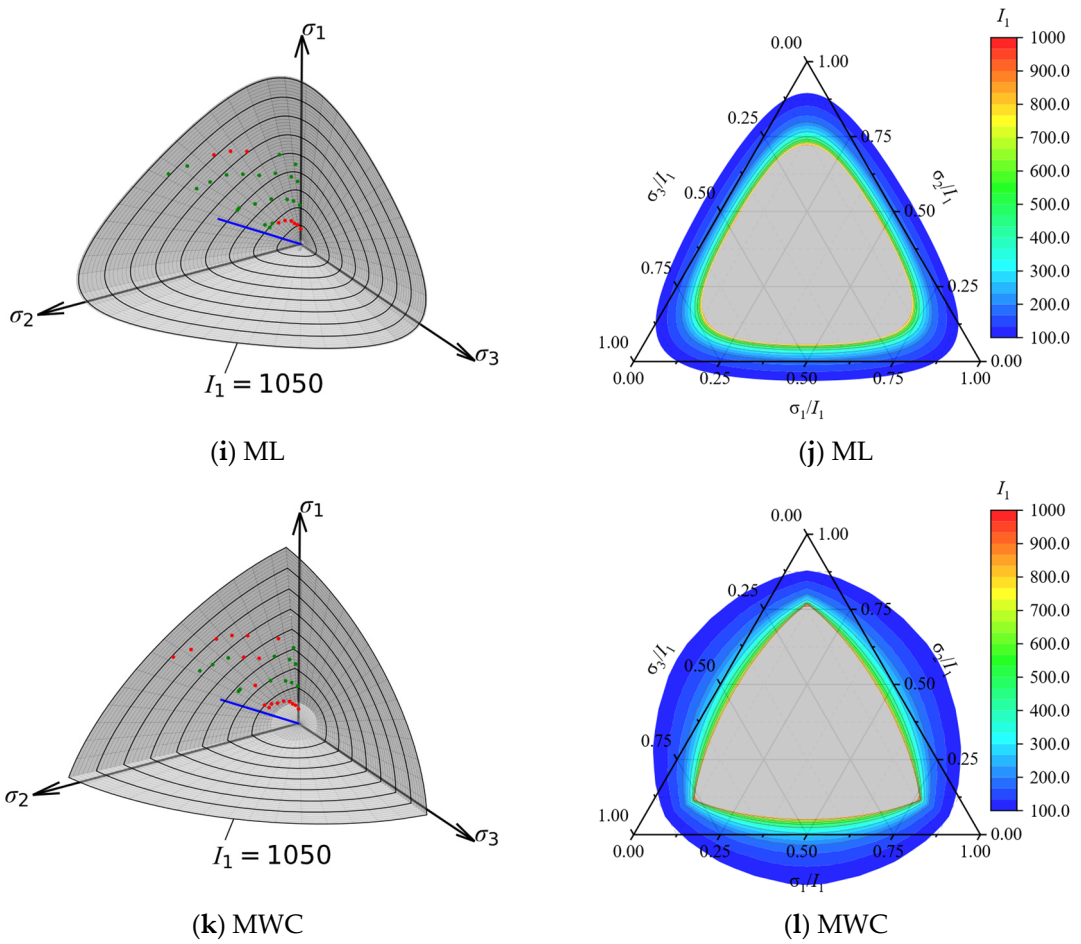

(**i**) ML (**j**) ML

(**k**) MWC (**l**) MWC

Figure 12. Envelope and ternary phases for the six models.

From Figure 12b, it can be observed that the deviatoric plane shape of the failure envelope of the HHO-MLP model gradually transitions from a triangle to a hexagon, which coincides with the Tresca strength criterion [56]. Meanwhile, at the same θ angle, the $\frac{\sigma_1}{I_1}$, $\frac{\sigma_2}{I_1}$, and $\frac{\sigma_3}{I_1}$ vary with the range of θ and the trend of I_1. Near $\theta = 0°$, the $\frac{\sigma_1}{I_1}$ decreases continuously as I_1 increases. Near θ = 60°, the $\frac{\sigma_1}{I_1}$, $\frac{\sigma_2}{I_1}$ and $\frac{\sigma_3}{I_1}$ gradually tend toward a constant value as I_1 increases. On the other hand, for the remaining five models, at the same θ, as I_1 increases, the ratios $\frac{\sigma_1}{I_1}$, $\frac{\sigma_2}{I_1}$, and $\frac{\sigma_3}{I_1}$ tend toward a constant value. Thus, it can be observed that for the HHO-MLP model, the growth trend of the triaxial strength in the compression region ($\theta = 0°$) decreases as I_1 increases, while the growth trend of the triaxial strength in the tension region ($\theta = 60°$) tends toward a constant value as I_1 increases. For the five strength criterion models, the growth trend of the triaxial strength within the same θ range becomes constant with the increase in I_1, and the shape of the model failure envelope on the deviatoric plane is relatively fixed, only expanding proportionally with the increase in I_1.

However, it is worth noting that, at certain I_1 levels, the failure envelope of the HHO-MLP model is not smooth at the CMB and TMB. Of course, only the ML and DP models satisfy this condition across all I_1 levels, while the other models exhibit this issue. Overall, from the perspective of the relationship between the failure envelope and the actual data points, the HHO-MLP model demonstrates significant advantages, with decent performance in terms of failure envelope continuity and smoothness. In the entire principal stress space, the HHO-MLP model successfully predicted the true triaxial strength of No. 10 sandstone. However, there are sharp points on the CMB and TMB of the envelope surface at certain I_1 levels, leading to discontinuities in the derivatives at these locations,

which could hinder its further application in numerical analysis. This can be solved by mathematical or numerical processing.

7. Conclusions

This study proposes a method for constructing a true triaxial strength model for sandstone using an MLP model. The HHO technique is employed to adjust the hyperparameters of the MLP model. By using the σ_c, σ_2, and σ_3 as inputs, the prediction of the true triaxial strength of sandstone is achieved. Crucially, the study ensures that the MLP model is continuously differentiable, meeting the requirements for numerical analysis by carefully adjusting the model's structure and activation function. Four distinct HHO-MLP models were trained using true triaxial strength data of sandstone with different activation functions. Instead of solely relying on prediction accuracy for model selection, an innovative comparison was conducted by analyzing the models on the meridional plane. This analysis excluded two models with strong prediction accuracy but significant discrepancies in the compressive and tensile meridian trends compared to theoretical expectations. Among the remaining models, the one that best aligned with theoretical trends while maintaining high prediction accuracy was chosen as the target HHO-MLP model. Five existing strength criteria were used as a comparison (DP, HB, MGC, ML, MWC). The results indicate that the HHO-MLP model outperforms the five existing strength criterion models on both the training and test sets. HHO-MLP shows better generalization performance for various sandstones under various stress conditions. In contrast, the predictions of σ_1 for the $\sigma_1 > 400$ MPa state by the traditional strength criteria all show large deviations, which indicates that the generalization performance of the traditional strength criteria is weak. At the same time, the large deviation in the traditional strength criteria in the high-stress zone suggests a change in the true triaxial strength behavior of the sandstone with increasing stress. The conventional strength criteria are limited by their structure and cannot predict this change process. Across the four evaluation metrics used, the HHO-MLP model slightly lags behind the MGC model in terms of MAPE on both the training and test sets, but outperforms the five strength criterion models in terms of R^2, RMAE, and MAE. This demonstrates the accuracy of the HHO-MLP model in predicting the true triaxial strength of sandstones at the stress states involved in the dataset.

With further analysis of the shape of the HHO-MLP model's envelope in the meridional plane, deviatoric plane, and principal stress space, it was observed that the compressive and tensile meridians of the HHO-MLP model align well with experimental data, and its development trend is similar to that of the HB, MGC, ML, and MWC models, except for minor differences in the compressive meridian under high S_8 conditions. On the deviatoric plane, the shape of the HHO-MLP model's failure envelope matches different strength criteria at various stress levels and generally meets the requirements of smoothness and continuity. A comparison in the principal stress space reveals that the HHO-MLP model predicts rock true triaxial strength conservatively, further validating the continuity and smoothness of the failure envelope. However, in the compressive region ($\theta = 0^\circ$), the predicted development trend of rock true triaxial strength by the HHO-MLP model differs from that of the other five strength criterion models as I_1 increases. Nonetheless, due to the lack of true triaxial test data for this rock in this region under high I_1, it is challenging to determine which trend better fits the actual situation.

In summary, this study demonstrates that the obtained HHO-MLP model outperforms the five existing strength criterion models in terms of prediction accuracy. Meanwhile, the HHO-MLP model has a better performance on the failure envelope and completely predicts the true triaxial strength of sandstone No. 10 in the principal stress space. However, there are sharp points on the CMB and TMB at certain I_1 levels, which affect the continuous differentiability in this region. Further mathematical or numerical processing is needed to solve the problem if the model is to be further extended and applied to numerical analysis. Future work will focus on refining the model to address the identified limitations and further improve its applicability in numerical analysis.

Author Contributions: R.Z., methodology, validation, resources, visualization, software, and writing—original draft; J.Z., conceptualization, methodology, validation, investigation, visualization, writing—review and editing, supervision, and funding acquisition; Z.W., formal analysis and writing—review and editing. All authors have read and agreed to the published version of the manuscript.

Funding: This research is partially supported by the National Natural Science Foundation of China (42177164; 52474121), the Distinguished Youth Science Foundation of Hunan Province of China (2022JJ10073), and the Outstanding Youth Project of the Hunan Provincial Department of Education (23B0008).

Institutional Review Board Statement: Not applicable.

Informed Consent Statement: Not applicable.

Data Availability Statement: The raw data supporting the conclusions of this article will be made available by the authors on request.

Conflicts of Interest: The authors declare that they have no known competing financial interests or personal relationships that could have appeared to influence the work reported in this paper.

References

1. Haimson, B. True triaxial stresses and the brittle fracture of rock. *Pure Appl. Geophys.* **2006**, *163*, 1101–1130. [CrossRef]
2. You, M. True-triaxial strength criteria for rock. *Int. J. Rock Mech. Min. Sci.* **2009**, *46*, 115–127. [CrossRef]
3. Zhou, H.; Liu, Z.; Liu, F.; Shao, J.; Li, G. Anisotropic strength, deformation and failure of gneiss granite under high stress and temperature coupled true triaxial compression. *J. Rock Mech. Geotech. Eng.* **2023**, *16*, 860–876. [CrossRef]
4. Winkler, M.B.; Frühwirt, T.; Marcher, T. Elastic Behavior of Transversely Isotropic Cylindrical Rock Samples under Uniaxial Compression Considering Ideal and Frictional Boundary Conditions. *Appl. Sci.* **2023**, *14*, 17. [CrossRef]
5. Vasyliev, L.; Malich, M.G.; Vasyliev, D.; Katan, V.; Rizo, Z. Improving a technique to calculate strength of cylindrical rock samples in terms of uniaxial compression. *Min. Miner. Depos.* **2023**, *17*, 43–50. [CrossRef]
6. Jiang, H.; Xie, Y. A note on the Mohr–Coulomb and Drucker–Prager strength criteria. *Mech. Res. Commun.* **2011**, *38*, 309–314. [CrossRef]
7. Hoek, E.; Brown, E.T. Empirical strength criterion for rock masses. *J. Geotech. Eng. Div.* **1980**, *106*, 1013–1035. [CrossRef]
8. Bieniawski, Z.T. Estimating the strength of rock materials. *J. S. Afr. Inst. Min. Metall.* **1974**, *74*, 312–320. [CrossRef]
9. Mogi, K. Fracture and flow of rocks under high triaxial compression. *J. Geophys. Res.* **1971**, *76*, 1255–1269. [CrossRef]
10. Chang, C.; Haimson, B. True triaxial strength and deformability of the German Continental Deep Drilling Program (KTB) deep hole amphibolite. *J. Geophys. Res. Solid Earth* **2000**, *105*, 18999–19013. [CrossRef]
11. Wu, S.; Zhang, S.; Zhang, G. Three-dimensional strength estimation of intact rocks using a modified Hoek-Brown criterion based on a new deviatoric function. *Int. J. Rock Mech. Min. Sci.* **2018**, *107*, 181–190. [CrossRef]
12. Schwartzkopff, A.K.; Sainoki, A.; Bruning, T.; Karakus, M. A conceptual three-dimensional frictional model to predict the effect of the intermediate principal stress based on the Mohr-Coulomb and Hoek-Brown failure criteria. *Int. J. Rock Mech. Min. Sci.* **2023**, *172*, 105605. [CrossRef]
13. Da Silva, M.V.; Antão, A. A new Hoek-Brown-Matsuoka-Nakai failure criterion for rocks. *Int. J. Rock Mech. Min. Sci.* **2023**, *172*, 105602. [CrossRef]
14. Drucker, D.C.; Prager, W. Soil mechanics and plastic analysis or limit design. *Q. Appl. Math.* **1952**, *10*, 157–165. [CrossRef]
15. Mogi, K. Effect of the intermediate principal stress on rock failure. *J. Geophys. Res.* **1967**, *72*, 5117–5131. [CrossRef]
16. Lade, P.V.; Duncan, J.M. Elastoplastic stress-strain theory for cohesionless soil. *J. Geotech. Eng. Div.* **1975**, *101*, 1037–1053. [CrossRef]
17. Zhou, S. A program to model the initial shape and extent of borehole breakout. *Comput. Geosci.* **1994**, *20*, 1143–1160. [CrossRef]
18. Ewy, R.T. Wellbore-stability predictions by use of a modified Lade criterion. *SPE Drill. Complet.* **1999**, *14*, 85–91. [CrossRef]
19. Zhang, L.; Zhu, H. Three-dimensional Hoek-Brown strength criterion for rocks. *J. Geotech. Geoenviron. Eng.* **2007**, *133*, 1128–1135. [CrossRef]
20. Zhang, Q.; Shuilin, W.; Xiurun, G.; Hongying, W. Modified Mohr-Coulomb strength criterion considering rock mass intrinsic material strength factorization. *Min. Sci. Technol.* **2010**, *20*, 701–706. [CrossRef]
21. Singh, M.; Raj, A.; Singh, B. Modified Mohr–Coulomb criterion for non-linear triaxial and polyaxial strength of intact rocks. *Int. J. Rock Mech. Min. Sci.* **2011**, *48*, 546–555. [CrossRef]
22. Zhang, R.; Zhou, J.; Tao, M.; Li, C.; Li, P.; Liu, T. Borehole Breakout Prediction Based on Multi-Output Machine Learning Models Using the Walrus Optimization Algorithm. *Appl. Sci.* **2024**, *14*, 6164. [CrossRef]
23. Fathipour-Azar, H. Polyaxial Rock Failure Criteria: Insights from Explainable and Interpretable Data-Driven Models. *Rock Mech. Rock Eng.* **2022**, *55*, 2071–2089. [CrossRef]
24. Yu, B.; Zhang, D.; Xu, B.; Liu, Y.; Zhao, H.; Wang, C. Modeling of true triaxial strength of rocks based on optimized genetic programming. *Appl. Soft Comput.* **2022**, *129*, 109601. [CrossRef]

25. Zhou, J.; Zhang, R.; Qiu, Y.; Khandelwal, M. A true triaxial strength criterion for rocks by gene expression programming. *J. Rock Mech. Geotech. Eng.* **2023**, *15*, 2508–2520. [CrossRef]
26. Rafiai, H.; Jafari, A.; Mahmoudi, A. Application of ANN-based failure criteria to rocks under polyaxial stress conditions. *Int. J. Rock Mech. Min. Sci.* **2013**, *59*, 42–49. [CrossRef]
27. Rukhaiyar, S.; Samadhiya, N.K. A polyaxial strength model for intact sandstone based on Artificial Neural Network. *Int. J. Rock Mech. Min. Sci.* **2017**, *95*, 26–47. [CrossRef]
28. Rafiai, H.; Jafari, A. Artificial neural networks as a basis for new generation of rock failure criteria. *Int. J. Rock Mech. Min. Sci.* **2011**, *48*, 1153–1159. [CrossRef]
29. Hong, H. Assessing landslide susceptibility based on hybrid multilayer perceptron with ensemble learning. *Bull. Eng. Geol. Environ.* **2023**, *82*, 382. [CrossRef]
30. Ding, K.; Fan, S.; Dong, S. Multilayer-perceptron-based prediction of sand-over-clay bearing capacity during spudcan penetration. *Int. J. Nav. Archit. Ocean Eng.* **2022**, *14*, 100479. [CrossRef]
31. Vinay, L.S.; Bhattacharjee, R.M.; Ghosh, N.; Kumar, S. Machine learning approach for the prediction of mining-induced stress in underground mines to mitigate ground control disasters and accidents. *Geomech. Geophys. Geo-Energy Geo-Resour.* **2023**, *9*, 159. [CrossRef]
32. Almeida, L.B. Multilayer perceptrons. In *Handbook of Neural Computation*; CRC Press: Boca Raton, FL, USA, 2020; pp. C1. 2: 1–C1. 2: 30.
33. Xu, Y.; Li, F.; Asgari, A. Prediction and optimization of heating and cooling loads in a residential building based on multi-layer perceptron neural network and different optimization algorithms. *Energy* **2022**, *240*, 122692. [CrossRef]
34. Heidari, A.A.; Mirjalili, S.; Faris, H.; Aljarah, I.; Mafarja, M.; Chen, H. Harris hawks optimization: Algorithm and applications. *Future Gener. Comput. Syst.* **2019**, *97*, 849–872. [CrossRef]
35. Yang, X.-S. *Nature-Inspired Metaheuristic Algorithms*; Luniver Press: Bristol, UK, 2010.
36. Hill, R. *The Mathematical Theory of Plasticity*; Oxford University Press: Oxford, UK, 1998; Volume 11.
37. Marinos, P.; Hoek, E. Estimating the geotechnical properties of heterogeneous rock masses such as flysch. *Bull. Eng. Geol. Environ.* **2001**, *60*, 85–92. [CrossRef]
38. Feng, F.; Li, X.; Du, K.; Li, D.; Rostami, J.; Wang, S. Comprehensive evaluation of strength criteria for granite, marble, and sandstone based on polyaxial experimental tests. *Int. J. Geomech.* **2020**, *20*, 04019155. [CrossRef]
39. Kwasniewski, M.; Takahashi, M.; Li, X. Volume changes in sandstone under true triaxial compression conditions. In Proceedings of the 10th ISRM Congress, Sandton, South Africa, 8–12 September 2003.
40. Pobwandee, T. Effects of Intermediate Principal Stress on Compressive Strength and Elasticity of Phra Wihan Sandstone. Master's Thesis, School of Geotechnology, Institute of Engineering, Suranaree University of Technology, Nakhon Ratchasima, Thailand, 2010.
41. Rukhaiyar, S.; Samadhiya, N.K. Strength behaviour of sandstone subjected to polyaxial state of stress. *Int. J. Min. Sci. Technol.* **2017**, *27*, 889–897. [CrossRef]
42. Takahashi, M.; Koide, H. Effect of the intermediate principal stress on strength and deformation behavior of sedimentary rocks at the depth shallower than 2000 m. In Proceedings of the ISRM International Symposium, Pau, France, 30 August–2 September 1989; p. ISRM–IS-1989-1003.
43. Walsri, C.; Poonprakon, P.; Thosuwan, R.; Fuenkajorn, K. Compressive and tensile strengths of sandstones under true triaxial stresses. In Proceedings of the 2nd Thailand Symposium on Rock Mechanics, Chonburi, Thailand, 12–13 March 2009; pp. 199–218.
44. Feng, X.-T.; Kong, R.; Zhang, X.; Yang, C. Experimental study of failure differences in hard rock under true triaxial compression. *Rock Mech. Rock Eng.* **2019**, *52*, 2109–2122. [CrossRef]
45. Gao, Y.-H.; Feng, X.-T.; Zhang, X.-W.; Feng, G.-L.; Jiang, Q.; Qiu, S.-L. Characteristic stress levels and brittle fracturing of hard rocks subjected to true triaxial compression with low minimum principal stress. *Rock Mech. Rock Eng.* **2018**, *51*, 3681–3697. [CrossRef]
46. Smart, B.; Somerville, J.; Crawford, B.R. A rock test cell with true triaxial capability. *Geotech. Geol. Eng.* **1999**, *17*, 157–176. [CrossRef]
47. He, P.-F.; Ma, X.-D.; He, M.-C.; Tao, Z.-G.; Liu, D.-Q. Comparative study of nine intact rock failure criteria via analytical geometry. *Rock Mech. Rock Eng.* **2022**, *55*, 3083–3106. [CrossRef]
48. Murlidhar, B.R.; Nguyen, H.; Rostami, J.; Bui, X.; Armaghani, D.J.; Ragam, P.; Mohamad, E.T. Prediction of flyrock distance induced by mine blasting using a novel Harris Hawks optimization-based multi-layer perceptron neural network. *J. Rock Mech. Geotech. Eng.* **2021**, *13*, 1413–1427. [CrossRef]
49. Huang, S.; Zhou, J. An enhanced stability evaluation system for entry-type excavations: Utilizing a hybrid bagging-SVM model, GP and kriging techniques. *J. Rock Mech. Geotech. Eng.* 2024; *in press*. [CrossRef]
50. Zhou, J.; Yang, P.; Peng, P.; Khandelwal, M.; Qiu, Y. Performance evaluation of rockburst prediction based on PSO-SVM, HHO-SVM, and MFO-SVM hybrid models. *Min. Metall. Explor.* **2023**, *40*, 617–635. [CrossRef]
51. Qiu, Y.; Zhou, J.; He, B.; Armaghani, D.J.; Huang, S.; He, X. Evaluation and interpretation of blasting-induced tunnel overbreak: Using heuristic-based ensemble learning and gene ex-pression programming techniques. *Rock Mech. Rock Eng.* **2024**, 1–29. [CrossRef]
52. Zhou, J.; Qiu, Y.; Armaghani, D.J.; Zhang, W.; Li, C.; Zhu, S.; Tarinejad, R. Predicting TBM penetration rate in hard rock condition: A comparative study among six XGB-based metaheuristic techniques. *Geosci. Front.* **2021**, *12*, 101091. [CrossRef]

53. Zhang, Y.L.; Qiu, Y.G.; Armaghani, D.J.; Monjezi, M.; Zhou, J. Enhancing rock fragmentation prediction in mining operations: A Hybrid GWO-RF model with SHAP interpretability. *J. Cent. South Univ.* **2024**, 1–14. [CrossRef]
54. Zhou, J.; Qiu, Y.; Zhu, S.; Armaghani, D.J.; Li, C.; Nguyen, H.; Yagiz, S. Optimization of support vector machine through the use of metaheuristic algorithms in forecasting TBM advance rate. *Eng. Appl. Artif. Intell.* **2021**, *97*, 104015. [CrossRef]
55. Taylor, K.E. Summarizing multiple aspects of model performance in a single diagram. *J. Geophys. Res. Atmos.* **2001**, *106*, 7183–7192. [CrossRef]
56. Krabbenhoft, K.; Lyamin, A. Generalised Tresca criterion for undrained total stress analysis. *Géotech. Lett.* **2015**, *5*, 313–317. [CrossRef]

Disclaimer/Publisher's Note: The statements, opinions and data contained in all publications are solely those of the individual author(s) and contributor(s) and not of MDPI and/or the editor(s). MDPI and/or the editor(s) disclaim responsibility for any injury to people or property resulting from any ideas, methods, instructions or products referred to in the content.